A Graphene Oxide and Copper-Centered Metal Organic Framework Composite as a Tri-Functional Catalyst for HER, OER, and ORR

*Maryam Jahan, Zhaolin Liu, and Kian Ping Loh**

A composite made from the assembly of graphene oxide (GO) and copper-centered metal organic framework (MOF) shows good performance as a tri-functional catalyst in three important electrocatalysis reactions, namely: the hydrogen evolution reaction (HER), oxygen evolution reaction (OER), and oxygen reduction reaction (ORR). One of the challenges in the area of electrocatalysis is to find an effective catalyst that will reduce, as well as generate, oxygen at moderate temperatures. The enhanced electrocatalytic properties and stability in acid of the GO-MOF composite is due to the unqiue porous scaffold structure, improved charge transport and synergistic interactions between the GO and MOF. In polymer electrolyte membrane fuel cell testing, the GO-incorporated Cu-MOF composite delivers a power density that is 76% that of the commercial Pt catalyst.

1. Introduction

With rising concerns about energy shortages, there are intense efforts worldwide to find renewable and green energy sources as alternatives to fossil fuels. Efficient catalysts for hydrogen evolution reaction (HER), oxygen evolution reaction (OER), and oxygen reduction reaction (ORR) are of paramount importance for electrochemical energy applications in fuel cells, batteries, and electrochemical water splitting.[1–4] However, the high cost of Pt catalysts commonly used for such applications restricts widespread applications. The ongoing search is for a non-Pt catalyst that can rival the performance of Pt.[5] Reduced graphene oxide (GO)-based materials have been studied extensively as electrode materials and catalyst supports due to their high electrical conductivity, high specific surface area, and very efficient charge transfer at the electrodes.[6–8] GO is bifunctional in the third dimension because it contains epoxy and hydroxyl functional groups on both sides of its surface.[9] GO sheets can be used as pillar connectors in metal organic frameworks (MOF). The incorporation of GO may overcome the poor electron-conductive properties of most MOFs, which exclude them from being used as electrode materials or electrocatalysts. Previous attempts to improve the electrical conductivity of MOFs hybrids include mixing them with conductive phases, such as carbon nanotubes, fuctionalized graphenes, and metal nanocrystals.[10–13] Although this can provide electron conduction at a macroscopic level, local charge transport is still limited in the MOF due to size-exclusion effects defined by the pore apertures. Therefore, our motivation is to explore whether the incorporation of GO as an integral component of the framework will lower the overpotential and improve the charge transfer properties.

Cu compounds exhibit biomimetic chemistry with O_2, such as the reductive activation of O_2 in enzymes and the protein laccase.[14–16] It is interesting to construct copper-based MOF on GO as an alternative to Pt-based electrodes. To date, most copper complexes have been studied in alkaline media[17–21] due to their corrosion and instability in acid media. To address the stability issue in acid, we designed a GO/copper–MOF hybrid structure which can coordinate with two strong electronegative ligands based on oxygen and nitrogen functional groups, thus leading to an improvement in the framework stability, especially when it is encapsulated by GO in acid media. GO sheets become an integral component of the MOF framework by acting as struts to link MOF nodes, besides serving as a good electron transfer mediator.

M. Jahan, Prof. K. P. Loh
Department of Chemistry
Graphene Research Centre
National University of Singapore
3 Science Drive 3, Singapore 117543
E-mail: chmlohkp@nus.edu.sg
Dr. Z. Liu
Institute of Materials Research & Engineering
3 Research Link, 117602
Department of Chemical and Environmental Engineering
National University of Singapore
10 Kent Ridge Crescent, Singapore

DOI: 10.1002/adfm.201300510

2. Result and Discussion

The chemical structures of the subunits in the assembled MOF are illustrated in **Scheme 1**. The MOF is created by linking copper nitrate trihydrate, 1,4-benzenedicarboxylic acid (*bdc*) and triethylene-diamine (*ted*), abbreviated as Cu-MOF, as illustrated in Scheme 1b. The secondary building unit (SBU) is a paddle-wheel $Cu_2(COO)_4(ted)_2$ unit as shown in Scheme 1c. Each paddle-wheel SBU is linked by *bdc* within the layer to form a 2D net parallel to the *xy* plane, which is further connected by *ted* molecules to produce the 3D framework. Generally, the octahedral geometry of SBU with six connections renders a

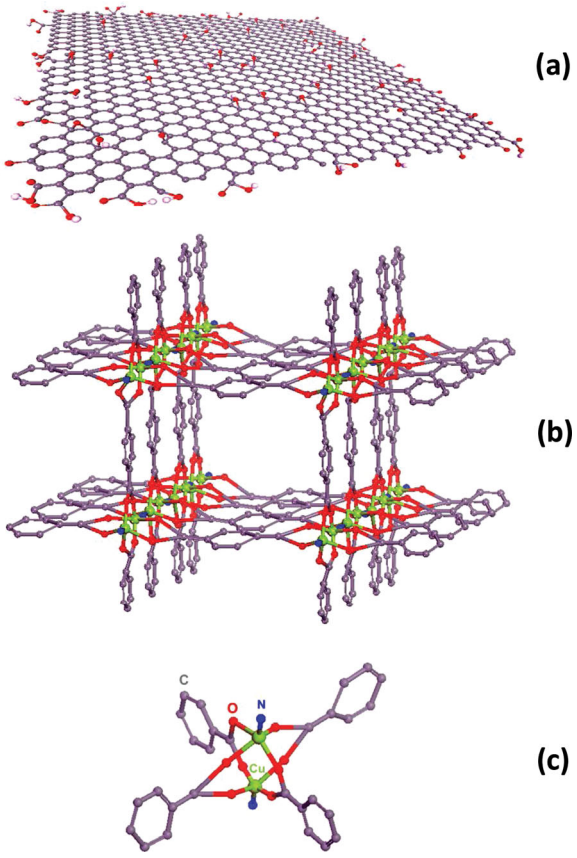

Scheme 1. Schematic of the chemical structures of: a) GO, b) Cu-MOF, and c) the paddle-wheel secondary building units of pure Cu-MOF.

cubic structure. Considering two different ligands (*bdc* and *ted*) at the apical and equatorial positions, the paddle-wheel unit is changed from the cubic structure to the tetragonal structure. The composite formed by the combination of GO and starting materials of pure MOF (*bdc*, *ted*, and $Cu(NO_3)_2$) is named as (GO *X* wt%) Cu-MOF where *X* indicate the weight percent of GO added into the composite. The improved catalytic performance of the composite can be expected based on two factors: i) the electron-accepting ability of the nitrogen and oxygen atoms, which polarizes the adjacent copper atom in the framework, and ii) the high surface area of GO, which also enhances the electron transfer during electrochemical reactions.

Cu-MOF, which is a 3D framework of the paddle-wheel unit, is synthesized by hydrothermal reaction. The structure-composition relationship was investigated by mixing different weight percentages of GO (2, 4, 6, 8 wt%) with the chemical precursors of Cu-MOF to synthesize (GO *X* wt%) Cu-MOF composites where $X = 2$, 4, 6, or 8 wt%. GO sheets decorated by OH and epoxy groups on either side of the sheets (Scheme 1a) are analogous to pillar connectors such as 1,4-benzene dicarboxylic acid used in classic MOF synthesis, which serve as bifunctional linkers for the paddle-wheel unit. The effects of GO on the crystallization and electrochemical properties of the MOF was studied systematically using optical absorption, vibrational spectroscopy, X-ray crystallography, cyclic voltammetry

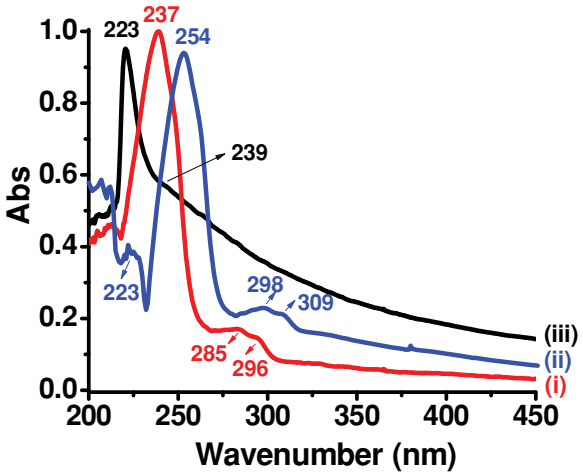

Figure 1. UV-vis absorption spectra of: i) Cu-MOF (3.5 mg L^{-1}), ii) (GO 8 wt%) Cu-MOF (3.2 mg L^{-1}), and iii) GO (2.5 mg L^{-1}) in methanol.

(CV), linear sweep voltammetry (LSV), rotating disk electrodes (RDE), and rotating ring disk electrodes (RRDE).

Figure 1 shows the UV-vis absorption spectra of GO, Cu-MOF, and (GO 8 wt%) Cu-MOF in methanol. The absorption peak of GO at 223 nm is due to the characteristic π-plasmon absorption[22–25] and a shoulder peak at about 239 nm, which could be assigned to the n to π transitions of C=O bonds. Cu-MOF shows absorption bands at 237 to 296 nm due to the π to π^* transition.[26,27] (GO 8 wt%) Cu-MOF shows a new band at 223 nm and a red shift in absorption bands compared to Cu-MOF. The presence of GO in (GO 8 wt%) Cu-MOF creates a new band at 223 nm assignable to the π to $\pi\alpha$ transitions of the aromatic domains in GO. A red shift in the absorption bands is characteristic of charge or energy transfer interaction between the poly aromatic scaffold in GO sheets and MOF.[28]

The functional groups present in GO, Cu-MOF and the composite are characterized by Fourier transform infrared (FTIR) spectroscopy (Figure S1, Supporting Information). Figure S2 (Supporting Information) shows an AC impedance spectroscopy study of (GO 8 wt%) Cu-MOF and pure Cu-MOF. The (GO 8 wt%) Cu-MOF shows smaller faradic impedance compared to Cu-MOF, confirming that GO can act as a good electron relay network. The thermal stability of (GO 8 wt%) Cu-MOF composite, Cu-MOF, and GO were examined by thermogravimetric analysis (TGA) (Figure S3, Supporting Information). In Figure S3b (Supporting Information), the weight loss at 100 °C originated from water molecules trapped inside the porosities. The mass reduction at around 250 °C was caused by the pyrolysis of the oxygen-containing functional groups in GO (Figure S3b, Supporting Information). The major mass reduction at ca. 450 °C was due to the structural collapse of MOF. In order to prove the presence of graphene sheet inside the framework, the encapsulated graphene was recovered from (GO 8 wt%) Cu-MOF sample and characterized by scanning electron microscopy (SEM), X-ray diffraction (XRD), atomic force microscopy (AFM), and Raman spectroscopy (Figure S4, Supporting Information).

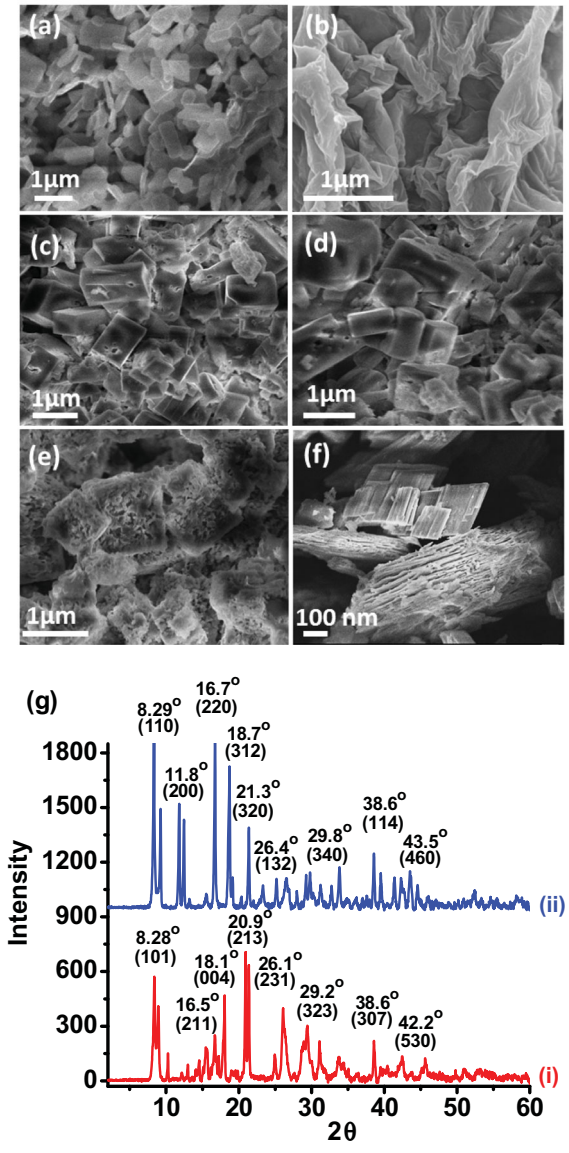

Figure 2. Evolution in the morphology and the crystal structure of the catalysts with different wt% of GO. SEM images for: a) Cu-MOF, b) GO, c) (GO 2 wt%) Cu-MOF, d) (GO 4 wt%) Cu-MOF, and e,f) (GO 8 wt%) Cu-MOF. g) XRD pattern of: i) Cu-MOF and ii) (GO 8 wt%) Cu-MOF. A peak at $2\theta = 11.8°$ is attributable to the enlarged interlayer spacing in GO and is visible also in the composite (GO 8 wt%) Cu-MOF.

The morphology evolution of GO, Cu-MOF crystal and (GO 2, 4, 8 wt%) Cu-MOF is shown in SEM images in **Figure 2**. It is interesting to see the marked change in the morphology of the MOF crystal with increasing concentration of GO incorporated in the MOF structure. The crystal phase of the composite was investigated by powder XRD (Figure 2e). Cu-MOF is assigned to the tetragonal crystal system with lattice parameter: $a = 15.811$ Å, $c = 19.976$ Å, space group: P4/*ncc* (No. 130). After adding 8 wt% of GO to the precursor of Cu-MOF, the lattice structure transforms into tetragonal space group with lattice parameters as follows: $a = 14.982$ Å, $c = 9.560$ Å, space group: P4/*mbm* (no. 127). Previously, Petit and Bandosz reported changes in the XRD pattern of MOF-5 with an increase in the content of GO, these were attributed to distortion of the cubic symmetry, however no new phases were reported.[11] The Cu-MOF synthesized here shares similar features to the $[Zn_2(1,4\text{-bdc})_2(dabco)]4DMF\cdot 1/2H_2O$ crystals (unit cell: I4/mcm) synthesized previously by Kim et al.[29] They reported the 1,4-*bdc* linker to be unusually bent, which results in severe twisting of the Zn_2 paddle wheel from an ideal square grid. Due to this distortion, the MOF crystals crystallize in a body-centered unit cell (I4/mcm) instead of a primitive cell with 4/mmm symmetry. This is a similar structure but with different phase compared to the P4/ncc phase of Cu-MOF. However, twisting of the COO^- groups around 10° has been observed in benzyl mono- and di-carboxylates in paddle-wheel structures.[30] Considering the high density of hydroxyl and epoxy groups on GO planes, the twisting of the *bdc* ligand arising from covalent bonding on GO planes may result in the phase transformation of MOF observed here, especially when a higher concentration of GO is added. As shown in the XRD spectum, a peak at $2\theta \approx 12°$, corresponding to a *d*-spacing of 8.14 Å, is attributable to the enlarged interlayer spacing in GO due to the presence of surface oxygen groups. The 002 reflections in GO is due to the poor ordering in the randomly stacked sheets.[31]

The electrocatalytic activity of the composite material was examined using cyclic voltammetry (CV) with 10 mM $Fe(CN)_6^{3-/4-}$ in 1 M KCl. As shown in **Figure 3**a, the incorporation of GO enhances the charge transfer kinetics by increasing the electroactive surface area of the material compared to bare glassy carbon (GC) electrode. The electroactive surface area can be estimated according to the Randles-Sevcik equation:

$$i_p = 2.99 \times 10^5 n A C D^{1/2} v^{1/2} \quad (1)$$

where i_p, n, A, C, D, and v are the peak current, the number of electrons involved in the reaction, the electroactive surface area, the concentration of the reactant, the diffusion coefficient of the reactant species, and the scan rate, respectively. The redox reaction of $Fe(CN)_6^{3-/4-}$ involves one-electron transfer ($n = 1$), and the diffusion coefficient (D) is 6.30×10^{-6} cm^2 s^{-1}. The electroactive surface area of (GO 8 wt%) Cu-MOF (8.92×10^{-2} cm^2) is 20 times larger than that of bare electrode (0.43×10^{-2} cm^2). The addition of GO also enhances the physical area for gas absorption, as confirmed by adsorption isotherm measurements. Comparison of CVs between GO and (GO 8 wt%) Cu-MOF in 10 mM $Fe(CN)_6^{3-/4-}$ in 1 M KCl is shown in Figure S5 (Supporting Information). The adsorption of N_2 follows a type I isotherm with Brunauer-Emmett-Teller (BET) surface areas of 1052, 821, and 776 m^2 g^{-1} for (GO 8 wt%) Cu-MOF, exfoliated reduced GO, and Cu-MOF, respectively (Figure 3b and Table S1, Supporting Information).

The electrochemical behavior of Cu-MOF, GO, and (GO 2 and 8 wt%) Cu-MOF was studied in 0.5 M H_2SO_4 solution using cyclic voltammetry (Figure 3c). In contrast to GO, which shows no distinctive redox peak in the scanned potential window, two redox peaks can be resolved in pure Cu-MOF and (GO 2 wt%) Cu-MOF, which are attributable to the redox reactions involving the Cu^{2+} center. By increasing GO ratio to 8 wt%, the anodic and cathodic current increases sharply and only one peak can be resolved, due to the fast electron transfer effect of GO.

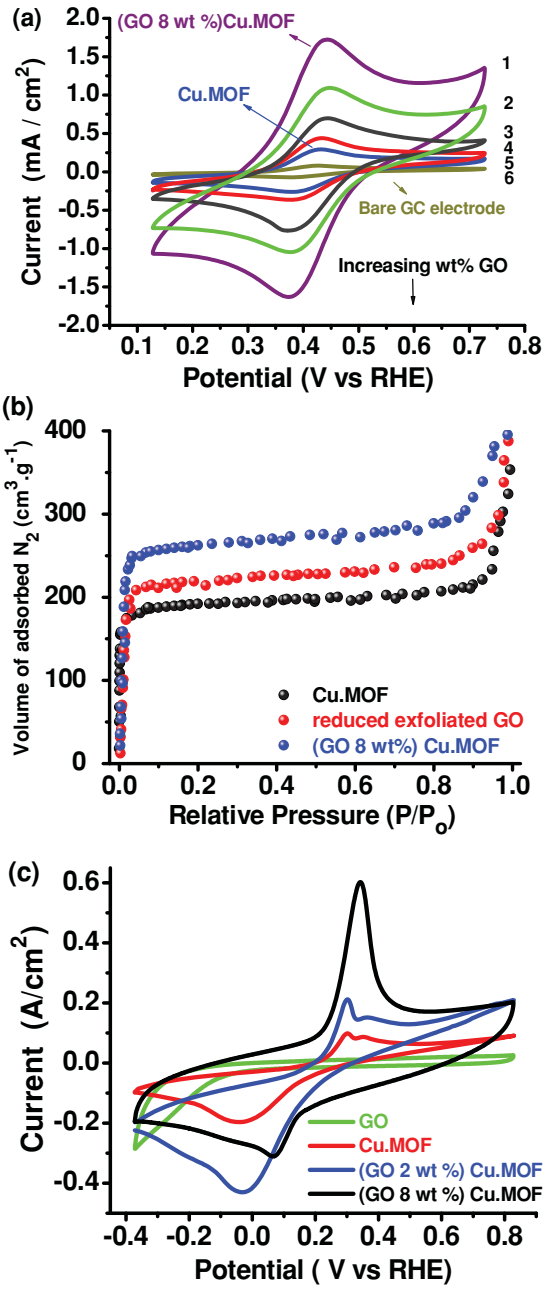

Figure 3. Electrochemical and sorption surface areas and electrochemical activity of the catalysts. a) Cyclic voltammograms of 10 mM $Fe(CN)_6^{3-/4-}$ in 1 M KCl using different materials drop casted on glassy carbon electrode: 1) (GO 8 wt%) Cu-MOF, 2) (GO 6 wt%) Cu-MOF, 3) (GO 4 wt%) Cu-MOF, 4) (GO 2 wt%) Cu-MOF, 5) Cu-MOF, and 6) bare glassy carbon electrode; the scan rate was 50 mV s^{-1}. b) Nitrogen gas sorption isotherms at 77 K for (GO 8 wt%) Cu-MOF, exfoliated reduced GO and Cu-MOF. P/P_0 is the pressure (P) to saturation pressure (P_0) with P_0 = 746 Torr. c) Cyclic voltammograms of catalysts drop casted on GC electrode; GO, Cu-MOF, (GO 2 wt%) Cu-MOF, and (GO 8 wt%) Cu-MOF in 0.5 M H_2SO_4; the scan rate was 50 mV s^{-1}.

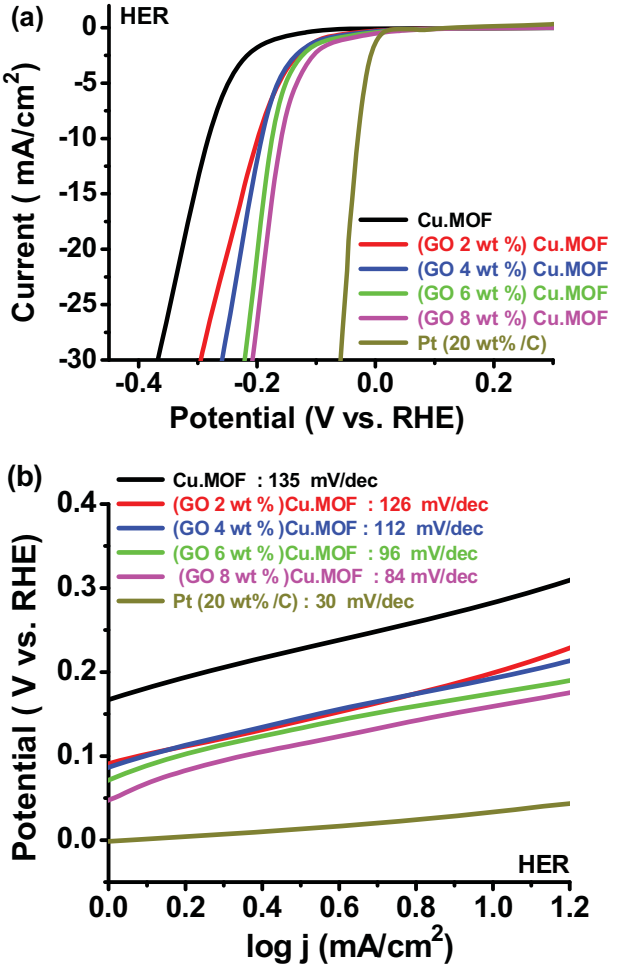

Figure 4. Hydrogen evolution reaction performance of the various catalysts. a) LSV polarisation curves of Pt/C, (GO 2, 4, 6, and 8 wt%) Cu-MOF, and Cu-MOF in 0.5 M H_2SO_4, N_2-saturated; scan rate: 2 mV s^{-1} at 25 °C. b) HER Tafel plots (log j versus potential for linear voltammetry) for Pt, (GO 2, 4, 6, and 8 wt%) Cu-MOF, and Cu-MOF in N_2-saturated 0.5 M H_2SO_4; scan rate: 2 mV s^{-1}.

The electrocatalytic activity of the hybrid samples for hydrogen evolution reaction (HER) was examined in N_2-saturated 0.5 M H_2SO_4 solution. HER was performed in a three-electrode electrochemical cell with the active film deposited on glassy carbon (GC) electrode. Linear sweep voltammograms (LSV) for HER in 0.5 M H_2SO_4 nitrogen-saturated solution were investigated for (GO 2, 4, 6, 8 wt%) Cu-MOF composites and pure Cu-MOF and compared with commercial Pt catalyst (20 wt% Pt on carbon black) (**Figure 4**a). The onset potential for HER is observed at –0.202 V for Cu-MOF, and the values decrease steadily from –0.123 to –0.087 V and approach the onset potential of Pt/C (0.013 V) as the composition of GO in the hybrid MOF increases from 2 to 8 wt%. (GO 8 wt%) Cu-MOF composite exhibits a high current density of 122.5 mA cm^{-2} at potential of –0.4 V (Figure S6, Supporting Information), which is higher than that of Cu-MOF although it is lower than Pt/C (313 mA cm^{-2}) at the same potential. The improved electrocatalysis exhibited by the (GO 8 wt%) Cu-MOF composite suggests smaller activation energy for HER in the presence of GO. The potential of the (GO 8 wt%) Cu-MOF

composite is around –0.20 V while the potential of Pt catalyst is –0.06 V at a current density of –30 mA cm^{-2}.

Based on the polarization curves presented in Figure 4b, the corresponding Tafel plots are constructed. An important parameter to evaluate the activity in HER is the Tafel slope (b) which is determined by fitting polarization data to the Tafel equation ($\eta = a + b \log |J|$, where η is the overpotential, b is the Tafel slope, and, J is the current density). The commercial Pt exhibits high HER catalytic activity with near zero overpotential and low Tafel slope of 30 mV dec^{-1}.[32] The b values for (GO 8 wt%) Cu-MOF electrode and Cu-MOF are 84 and 135 mV dec^{-1}, respectively. The Tafel slope of 126 mV dec^{-1} for (GO 2 wt%) Cu-MOF agrees well with the theoretically expected Tafel slope ($2.3 \times 2RT/F$) with the assumption that the Volmer reaction is rate limiting.[32] By tuning the ratio of GO to MOF, we find that (GO 8 wt%) Cu-MOF exhibits the highest HER activity with a small overpotential, high current density and a low Tafel slope of 84 mV dec^{-1}. This result is better than ternary copper–molybdenum-sulfide (Cu_2MoS_4) (Tafel slope: 95 mV dec^{-1}, overpotential of –0.35 V at –12 mA cm^{-2}).[33]

The potential of our hybrid material for electro catalytic oxygen evolution reaction (OER) is examined next. The LSV of electrodes measured at a low scan rate of 2 mV s^{-1} at 25 °C is shown in **Figure 5**a. The onset potential of (GO 8 wt%) Cu-MOF is 1.19 V, whereas the onset potential of Cu-MOF appeared at 1.39 V. Observing potential of 1.43 V at 2 mA cm^{-2} for Pt/C compared to 1.34 V for the composite (GO 8 wt%) Cu-MOF reveals that the composite is very active for OER in acid media. However, the current density of Pt/C of 12.5 mA cm^{-2} is more than two times that of (GO 8 wt%) Cu-MOF at 5.8 mA cm^{-2} with the same loaded sample (Figure S7, Supporting Information).

The kinetics of the OER for (GO 2, 4, 6, and 8 wt%) Cu-MOF electrodes were determined by recording Tafel polarization (E vs log j) curves at a slow scan rate (2 mV s^{-1}). Each curve, as shown in Figure 5b, displays two Tafel slopes, one at low overpotential and the other at high overpotential. At low overpotential, the Tafel slope is 65 mV dec^{-1} for (GO 8 wt%) Cu-MOF, whereas the slope is 89 mV dec^{-1} for Cu-MOF. In this case, the Tafel slope of (GO 8 wt%) Cu-MOF matches the Tafel slope of Pt/C (61 mV dec^{-1}). The Tafel slope of (GO 8 wt%) Cu-MOF (157 mV dec^{-1}) is lower than Cu-MOF (211 mV dec^{-1}) in high overpotential ranges, indicating better catalytic activity for this composite. The results are summarized in **Table 1**. The finding is consistent with what was observed in the HER, a higher concentration of GO (8 wt%) in the hybrid facilitates the OER.

Another electro-reduction reaction is the oxygen reduction reaction (ORR) which is tested in 0.5 M H_2SO_4 solution (saturated with either nitrogen or oxygen) (Figure S8a, Supporting Information). There is a significant enhancement of the cathodic peak at –0.23 V (vs Ag/AgCl) in O_2-saturated H_2SO_4 for (GO 8 wt%) Cu-MOF whereas such a peak is absent in N_2-saturated solution. Since typical Pt/C commercial catalyst is prone to methanol poisoning, we assessed the methanol crossover effect (Figure S8a,b, Supporting Information). In an electrolyte (0.5 M H_2SO_4) saturated with O_2 and containing 3 M methanol, the cathodic peaks for oxygen reduction disappear in Pt-catalyst loaded GC electrode, and a strong methanol

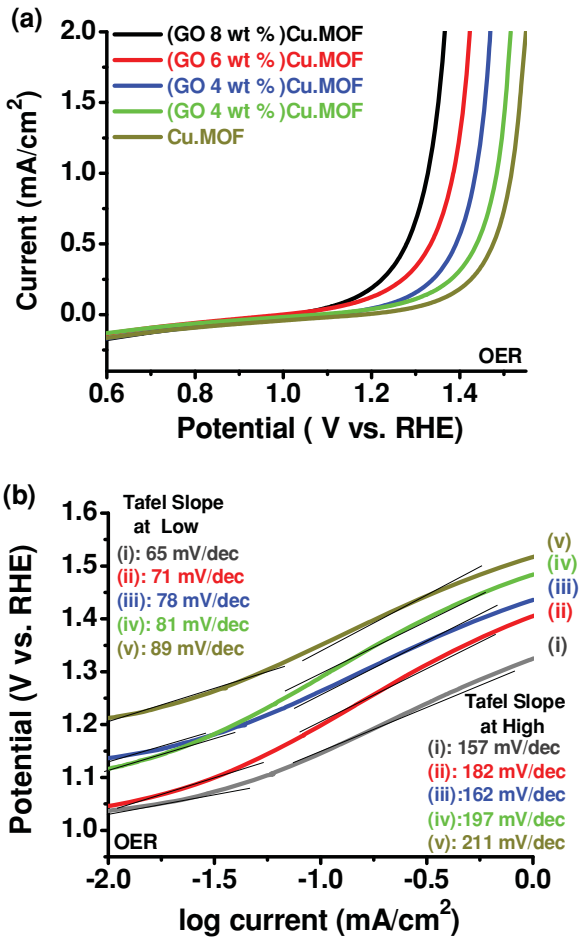

Figure 5. Oxygen evolution reaction performance of the various catalysts. a) LSV polarisation curves for Cu-MOF, (GO 2, 4, 6, and 8 wt%) Cu-MOF in N_2-saturated 0.5 M H_2SO_4; scan rate: 2 mV s^{-1} at 25 °C. b) OER Tafel plots (log j versus potential for linear voltammetry) for: i) (GO 8 wt%) Cu-MOF, ii) (GO 6 wt%) Cu-MOF, iii) (GO 4 wt%) Cu-MOF, iv) (GO 2 wt%) Cu-MOF, and v) Cu-MOF in N_2-saturated 0.5 M H_2SO_4; scan rate: 2 mV s^{-1}.

oxidation peak is observed instead (Figure S8b, Supporting Information). In contrast, no activity specific to methanol is observed and the characteristic peaks of ORR is maintained in (GO 8 wt%) Cu-MOF, which indicates that the latter is tolerant to methanol (Figure S8a, Supporting Information). To investigate the performance of the catalyst for ORR, various composites were drop-casted on glassy carbon electrode. In Figure S9 (Supporting Information), the reduction potential for ORR is shifted increasingly to more positive values with a higher wt% of GO in the MOF. The cathodic peak for ORR in (GO 8 wt%) Cu-MOF- modified cathode is shifted positively to –0.23 V and the ORR current density at –0.97 mA cm^{-2} of the composite is the highest among the samples.

The corresponding Koutecky-Levich plots (j^{-1} vs $\omega^{-1/2}$) at various electrode potentials show good linearity (**Figure 6**a). Linearity and parallelism of the plots are considered as typical of first-order reaction kinetics with respect to the concentration of dissolved O_2. The kinetic parameters can be analyzed on the basis of the Koutecky-Levich equations:

Table 1. Electrochemical parameters of HER, OER, and ORR.

Reaction	Parameters	Cu-MOF	(GO 6 wt%) Cu-MOF	(GO 8 wt%) Cu-MOF	Pt
HER	Tafel slop (mV dec^{-1})	135	96	84	30
	Overpotential (V vs. RHE) at –30 mA cm^{-2}	–0.369	–0.222	–0.209	–0.058
	Onset potential (V vs. RHE)	–0.202	–0.104	–0.087	0.013
	–Current density (mA cm^{-2}) at –0.4 V	39.12	104.71	122.48	313.11
OER	Tafel slop b1 (mV dec^{-1})	89	71	65	61
	Tafel slop b2 (mV dec^{-1})	211	182	157	122
	Overpotential (V vs. RHE) at 2 mA cm^{-2}	1.54	1.42	1.34	1.43
	Onset potential (V vs. RHE)	1.39	1.22	1.19	1.30
	Highest current density (mA cm^{-2})	2.1	4.2	5.8	12.5
ORR	Tafel slop b1 (mV dec^{-1})	98	79	69	60
	Tafel slop b2 (mV dec^{-1})	196	142	132	121
	Overpotential (V vs. RHE) at –1.1 mA cm^{-2}	–0.21	–0.09	–0.03	0.82
	Onset potential (V vs. RHE)	0.16	0.24	0.29	0.90
	– Current density (mA cm^{-2}) at –0.4 V	1.10	3.73	5.32	6.17

$$\frac{1}{j} = \frac{1}{j_L} + \frac{1}{j_K} = \frac{1}{B\omega^{1/2}} + \frac{1}{j_K} \quad (2)$$

$$B = 0.62nFC_0(D_0)^{2/3}\nu^{-1/6} \quad (3)$$

$$j_K = nFkC_0 \quad (4)$$

in which j is the measured current density, j_K and j_L are the kinetic and diffusion-limiting current densities, ω is the angular velocity of the disk ($\omega = 2N\pi N$, where N is the linear rotation speed), n is the overall number of electrons transferred in oxygen reduction, F is the Faraday constant (F = 96485 C mol^{-1}), C_0 is the bulk concentration of O_2, ν is the kinematic viscosity of the electrolyte, and k is the electron transfer rate constant. The number of electrons transferred (n) and j_K can be obtained from the slope and intercept of the Koutecky-Levich plots, respectively, and by using parameters $C_0 = 1.1 \times 10^{-6}$ mol cm^{-3}, $D_0 = 1.4 \times 10^{-5}$ cm s^{-1}, and $\nu = 0.01$ cm^2 s^{-1} in 0.5 M H_2SO_4, 25 °C, 1 atm. Investigation of the detailed electron transfer kinetics by rotating disk voltammetry shows a facile four-electron transfer kinetics similar to ORR catalyzed by Pt/C ($n \approx 4e^-$)[34] for a wide range of potential from –0.2 to –0.4 V (vs. RHE) for (GO 8 wt%) Cu-MOF, whereas the electron transfer number varies between 2 to 4 for Cu-MOF and GO from 0.15 V to –0.4 V (Figure S10d, Supporting Information). To determine the reaction order with respect to O_2, the rotation rate of the electrode was varied in the potential range corresponding to mixed activation-diffusion control zone (Figure 6b). In this way, the O_2 concentration is changed in the vicinity of the electrode surface whereas in the bulk solution it remains unaltered. By varying the rotation rate, the reaction order can be determined from the slope of the plot log j vs log $(1 - j/j_L)$:

$$\log j = \log j_K + m\log(1 - j/j_L) \quad (5)$$

where j_K is the kinetic current, j_L is the diffusion limiting current, and m is the reaction order with respect to dissolved oxygen molecules. In all cases the plot log j vs log $(1 - j/j_L)$ gave a fairly good straight line, as shown in Figure 6b. The slopes of the straight lines in this plot are close to one, 1, which indicates that there is a single-electron transfer process to the adsorbed oxygen on the electrode surface, following the reaction $(O_2)_{ads} + H^+ + e^- \rightarrow (HO_2)_{ads}$ as the rate-determining step.[35,36]

Figure 6c shows the mass transport-corrected Tafel plots for the oxygen reduction kinetics studies conducted in 0.5 M H_2SO_4 O_2-saturated at 25 °C. The Tafel plots were obtained after the measured currents were corrected for diffusion to give the kinetic currents in the mixed activation-diffusion region, calculated from:

$$j_K = j\ j_L/(j_L - j) \quad (6)$$

where $j_L/(j_L - j)$ is the mass transfer correction term.[37] The mass transport correction was made using the limiting current $j_L = B\ \omega^{1/2}$ where ω is the rotation rate. The kinetic parameters deduced for the oxygen reduction are presented in Table 1. Oxygen reduction occurred by different mechanisms in low and high current density regions. In the low current density region, the Tafel slope for (GO 8 wt%) Cu-MOF is 69 mV dec^{-1}, while in the high current density regions the slope is 132 mV dec^{-1}. For O_2 reduction by Pt in acid, a Tafel slope of 60 mV dec^{-1} can be obtained[38] and there is no detectable amount of peroxide measured indicating that O_2 reduction occurred by the four-electron pathway.[34] The change of Tafel slope from 69 to 132 mV dec^{-1} suggests a change in the reaction mechanism from Temkin-type adsorption at low current to Langmuir adsorption condition at high current.[38–41]

Figure 7 compares the ORR kinetics of the various synthesized samples. The onset potential for ORR is the first to be reached in the (GO 8 wt%) Cu-MOF (at 0.29 V vs. RHE) and the oxygen reduction current density of this electrode, at –5.3 mA cm^{-2}, is higher than the rest of the composites and the reduction potential has shifted to more positive

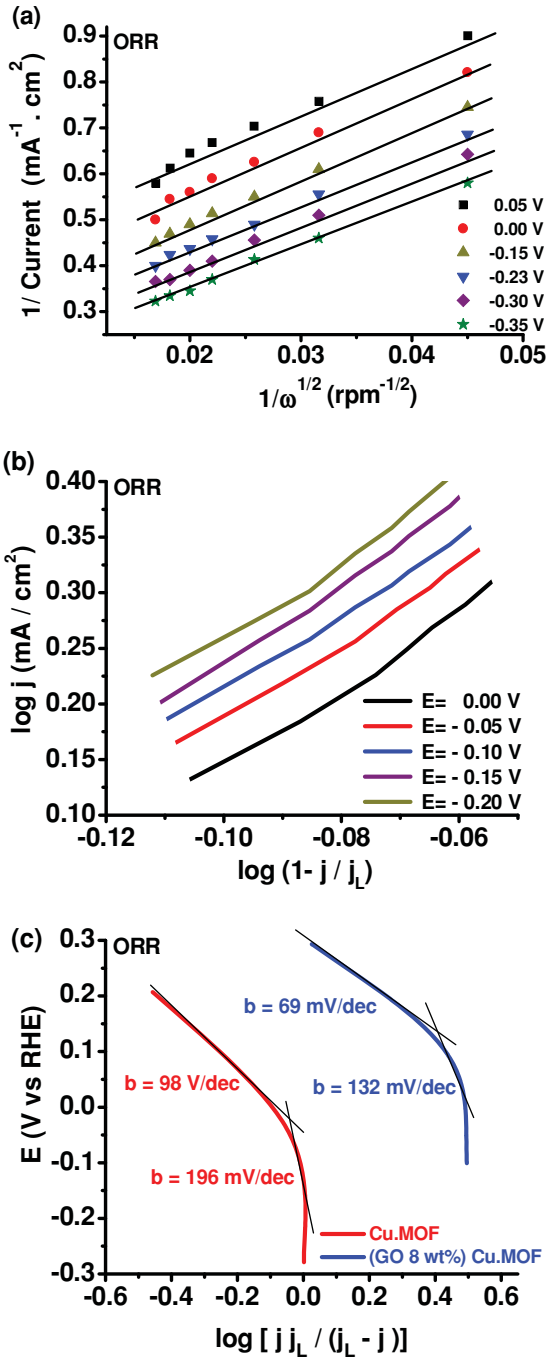

Figure 6. Kinetic study of ORR. a) Koutecky-Levich plots of (GO 8 wt%) Cu-MOF at different electrode potentials. b) Plots for the determination of the reaction order with respect to O_2 for ORR on (GO 8 wt%) Cu-MOF electrode. c) Mass transfer-corrected Tafel plots for ORR on (GO 8 wt%) Cu-MOF and Cu-MOF electrodes.

potentials. Once again, this suggests that the incorporation of GO into the MOF improves the electrocatalytical behavior. However, increasing the GO content to 20 wt% resulted in a decrease electrocatalytic activity due to dilution effect and loss of the crystallinity (Figure S11 and S12, and Table S2, Supporting Information). Importantly, our

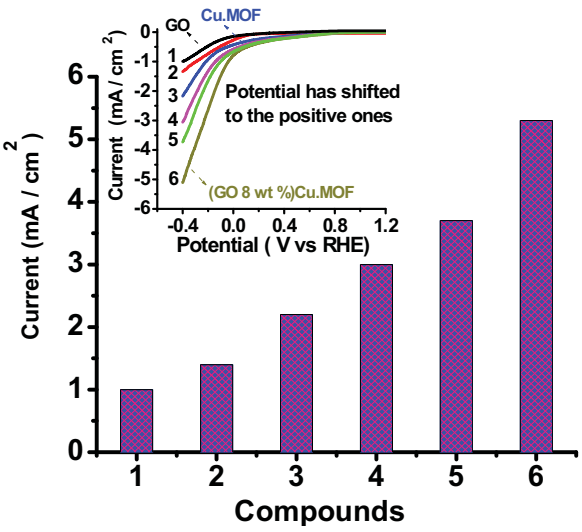

Figure 7. Comparison of ORR performance among various catalysts. Comparing ORR current density of: 1) GO, 2) (graphene 2 wt%) Cu-MOF (composite of unfunctionalized graphene and Cu-MOF], 3) Cu-MOF, 4) (GO 4 wt%) Cu-MOF, 5) (GO 6 wt%) Cu-MOF, and 6) (GO 8 wt%) Cu-MOF. The inset shows the corresponding ORR RDE voltammograms at a rotation rate of 3500 rpm (scan rate 2 mV s^{-1}).

catalyst exhibits good stability and durability compared to Pt/C in acid media (Figure S13, S14, and S15, Supporting Information).

To further examine the ORR catalytic pathways of our composite, we carried out rotating ring-disk electrode (RRDE) measurement in order to monitor the peroxide species formation during the process. **Figure 8**a gives the RRDE polarization curves for O_2 reduction on the Cu-MOF and (GO 8 wt%) Cu-MOF in 0.5 M H_2SO_4 saturated with oxygen. The H_2O_2 yield and the number of electrons transferred during the process can be determined by the followed equations:

$$n = 4N.I_D/(N.I_D + I_R) \quad (7)$$

$$\%H_2O_2 = 200I_R/(N.I_D + I_R) \quad (8)$$

$$N = -I_R/I_D \quad (9)$$

Where I_D is disk current, I_R is ring current, and N is current collection efficiency. Figure 8b shows the H_2O_2 yield on the catalysts. The measured H_2O_2 yields are below 50% and 20% for Cu-MOF and (GO 8 wt%) Cu-MOF, respectively. The RRDE results confirm our results calculated from the Koutecky-Levinch equation that the ORR electron number is close to 4 between –0.1 to –0.4 V for the (GO 8 wt%) Cu-MOF, but about between 2 to 4 for the Cu-MOF over the same potential range (Figure 8c).

Based on the ORR response, the electrocatalytic performance of GO/Cu-MOF composites in a single polymer electrolyte membrane fuel cell (PEMFC) was evaluated. In order to compare the performance, the same mass of Cu (2.7 mg Cu cm^{-2}) was used in all samples. The anode was made of 0.8 mg Pt cm^{-2} mixed with carbon black. For the control sample, 1.8 mg cm^{-2} wt% Pt was loaded at the

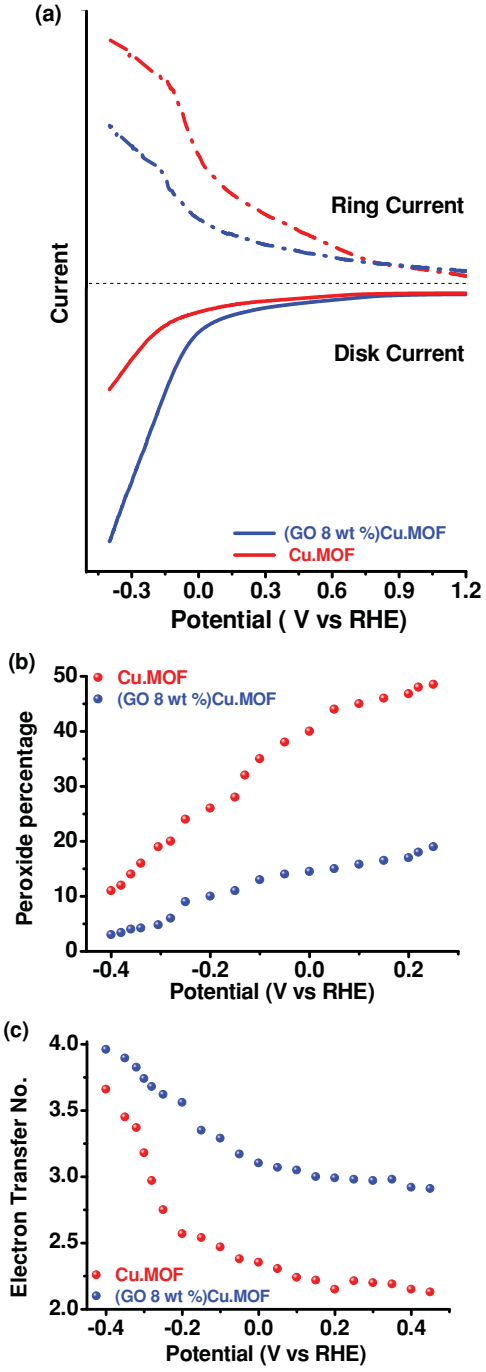

Figure 8. Investigation of peroxide percentage and electron transfer number in ORR catalyzed by various catalysts.. a) Rotating ring–disk electrode voltammograms recorded for Cu-MOF and (GO 8 wt%) Cu-MOF electrodes in O_2-saturated 0.5 M H_2SO_4 at 3500 rpm (scan rate 2 mV s^{-1}). b) Peroxide percentage of Cu-MOF and (GO 8 wt%) Cu-MOF at different potentials calculated from RRDE measurement. c) The electron transfer number (*n*) of Cu-MOF and (GO 8 wt%) Cu-MOF at various potentials based on the corresponding RRDE data in (a).

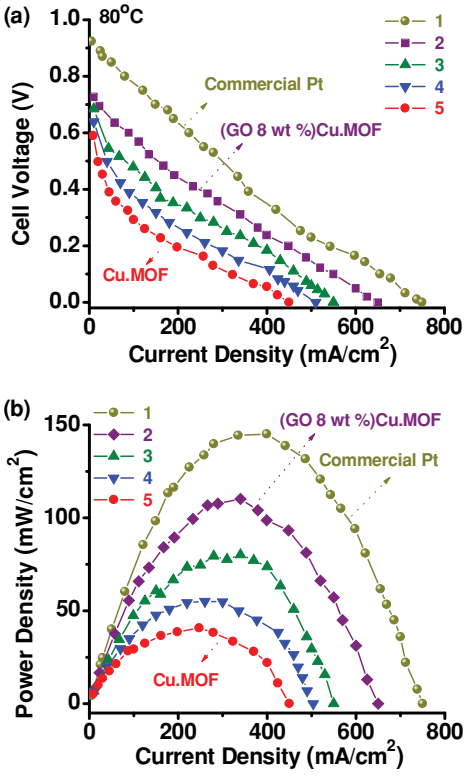

Figure 9. PEMFC study of the (GO X wt%) Cu-MOF composite compared with Pt/C. a) Polarization, and, b) power-density curves for the H_2/O_2 fuel cell MEAs operating at 80 °C with different cathodes catalysts: 1) 20 wt.% Pt/C, 2) (GO 8 wt%) Cu-MOF, 3) (GO 6 wt%) Cu-MOF, 4) (GO 4 wt%) Cu-MOF, and (5) Cu-MOF.

cathode. **Figure 9**a shows the current density versus cell voltage of a single cell obtained for membrane electrodes assembly (MEA). The polarization curve of (GO 4, 6, and 8 wt%) Cu-MOF is higher than that of Cu-MOF in the low and high current region, which reveals the catalytic activity of the composite is higher than pure MOF. The open circuit voltages for (GO 8 wt%) Cu-MOF is 0.73 V while that of Pt is 0.93 V. Figure 9b shows the power density curves using Cu-MOF, (GO 4, 6, and 8 wt%) Cu-MOF and commercial 20 wt% Pt/C as the catalysts for the cathodes. A maximum power density of 145.2, 110.5, and 40.4 mW cm^{-2} was achieved for Pt, (GO 8 wt%) Cu-MOF, and Cu-MOF, respectively. Although the power density of the Cu-MOF composite cathodes is only 76% that of Pt/C catalyst, its performance as a lower cost substitute is quite comparable to previous reports using non-precious catalysts.[42–46]

The higher catalytic activities of our composites compared to pure MOF or GO alone for all electrochemical reactions (HER, OER, and ORR) should be attributed to the synergistic effects of framework porosity, a larger bond polarity due to oxygen ligand in the GO, and the catalytically active copper in the hybrid MOF. Physically mixing the Cu-MOF and GO gave relatively poorer response in ORR and OER (Figure S16, Supporting Information) compared to the GO-incorporated Cu-MOF. GO plays the role of a charge sink to allow rapid charge transfer in redox reaction, especially at the covalently bonded interface between the Cu-MOF and GO.

To date, there are many reports of non-precious metal-based bifunctional catalysts such as manganese oxide,[47] Co_3O_4/N-rmGO catalyst,[48] nickel electrodes,[49] and boron-doped diamond electrodes.[50] Recently, Cu-based MOF/graphene oxide composites have been used for the reactive adsorption of ammonia at room temperature,[51] and also for hydrogen adsorption.[52] Other kinds of MOFs (MOF-5, HKUST-1 or MIL-100(Fe))/GO composites have been tested for the removal of NH_3, H_2 S, and NO_2.[53,54] Here, we demonstrate a Cu-MOF/GO composite as a tri-functional catalysts for HER, ORR, and water oxidation/OER. Our work confirms that the incorporation of GO in MOF helps to improve the stability and catalytic performance of the composites in electrocatalysis. The synergistic interactions of GO and non-precious metal-based MOF afford a new path for energy conversion technologies based on earth-abundant, scalable, and non-precious metal catalysts.

3. Conclusions

We have investigated GO-incorporated Cu-MOF composite as a tri-functional catalyst for ORR, OER, and HER. The GO-incorporated Cu-MOF composites exhibit smaller overpotentials and higher current for all three electrocatalytic reactions and show better stability in acid media compared to pure MOF. In PEM fuel cell testing, the GO-incorporated Cu-MOF composite delivers power density that is 76% that of the commercial Pt catalyst. The fact that GO-incorporated Cu-MOF hybrid shows high electrocatalytic activity and stability combined with its low cost and facile synthesis suggests that it can be a promising alternative to Pt catalyst in fuel cell applications.

4. Experimental Section

Reagents and Chemicals: All chemicals were purchased from Sigma-Aldrich of the purest quality and used without further purification.

*Graphene Oxide (*GO): GO was prepared using a modified Hummers and Offeman's method. In a typical reaction, 0.5 g of graphite, 0.5 g of $NaNO_3$, and 23 mL of H_2SO_4 were stirred in an ice bath for 30 min. Next, 4 g of $KMnO_4$ was slowly added. The solution was heated to 35 ± 5 °C in a water bath and stirred for about 2 h; a thick green paste formed during this step. Then, 40 mL of water was added very slowly followed with stirring for 1 h while the temperature was raised to ca. 90 ± 5 °C. Finally, 100 mL of water was added followed by the slow addition of 3 mL of H_2O_2 (30%). The solution color turned from dark brown to pale yellowish brown. The warm solution was then filtered and washed with 100 mL water several times to adjust its pH at 7. The final product was stored under vacuum for drying.

Cu-MOF: Copper nitrate trihydrate (0.740 g), 1,4-benzenedicarboxylic acid (0.680 g) and triethylene-diamine (0.480 g) were dissolved in 150 mL DMF. The final mixture was sealed in a small capped Teflon vial and sonicated to ensure homogeneity. The autoclave vial was heated at 120 °C in an oven for 36 h followed by slow cooling to room temperature. The blue crystals were collected via filtration and washed with DMF several times and dried under vacuum.

GO (2, 4, 6, and 8 wt%) Cu-MOF: Copper nitrate trihydrate (0.740 g), 1,4-benzene dicarboxylic acid (0.680 g) and triethylene diamine (0.480 g) were dissolved in 150 mL DMF. Different amounts of GO (2, 4, 6, and 8 wt%: based on the total mass of starting solid materials) were added to the mixtures. After sonication of the solution, the final mixture was transferred into a small Teflon-capped autoclave. The autoclave was heated at 120 °C in an oven for 36 h followed by slow cooling to room temperature. The blue-grayish crystals were collected filtrated and washed with ample DMF and dried under vacuum.

Instrumentation: SEM images were recorded using a JEOL 6701 FESEM (field emission scanning electron microscope) at 30 kV. FT-IR spectroscopy measurements were recorded at room temperature on a Varian 3100 FT-IR spectrometer. The samples were ground with KBr and then pressed into disks. UV-vis spectroscopic data was collected using a UV-3600 Shimadzu UV-vis Spectrophotometer. Powder XRD diffraction was carried out using a Siemens D5005 X-ray diffractometer with CuKa line (l = 1.54060 Å) as the incident beam, calibrated by SiO_2. A Gobel mirror was employed as a monochromator. The sample powder was ground and then loaded into a glass holder and leveled with a glass slide before mounting it on the sample chamber. The specimens were scanned from 1.4–60°. The scan step-width was set to 0.005° and the scan rate to 0.005° s^{-1}. XRD data analysis was performed using Reflex module in Materials Studio (Accelrys) software suites. XRD patterns were indexed using the program X-Cell in Materials Studio (Accelrys) software.

All the electrochemical measurements were carried out in a polytetrafluoroethylene (PTFE) house (V = 5 mL) at room temperature using a three-electrode system with GC electrode as working electrode, Pt wire as counter electrode, and 1 M KCl-Ag/AgCl as reference electrode (using Autolab PGSTAT30 digital potentiostat/galvanostat). Cyclic voltammetetry (CV) was typically performed at a scan rate of 50 mV s^{-1}. The cyclic voltammogram experiments were conducted in either N_2- or O_2-saturated 0.5 M H_2SO_4 solution. RDE and RRDE experiments were carried out on a RRDE-3A (ALS Co., Ltd) and the CH instruments electrochemical workstation (CH instrument, Inc. Austin) bipotentiostat. RDE measurements were performed at rotation rates varying from 500 to 3500 rpm and with the scan rate of 2 mV s^{-1}. Linear sweep voltametry was performed at glassy carbon disk electrode with a 3 mm diameter Pt electrode, and Ag/AgCl reference electrode. For RRDE measurement, a Pt ring/GC disk electrode was used. Prior to use, the working electrode was polished mechanically with diamond down to an alumina slurry to obtain a mirror-like surface and then washed with deionized (DI) water and acetone and allowed to dry. Then, 8 mg of catalyst and 80 µL of 5 wt% Nafion solution were dispersed in 1 mL of 4:1 v/v water/ethanol with at least 30 min sonication to form a homogeneous ink. Then 2 µL of the catalyst ink (containing 16 µg of catalyst) was loaded onto glassy carbon electrode. The electrode was allowed to dry at room temperature for 30 min in a desiccator before measurement. After drying, a catalyst loading of 226.3 µg cm^{-2} was obtained. All the potentials reported are against the reversible hydrogen electrode (RHE).

In order to measure their fuel-cell properties, the Nafion 1135 membrane was used and cleaned by being immersed in boiling 35% H_2O_2 for 45 min, and then in boiled 1 M H_2SO_4 for 45 min. The membrane was then rinsed in boiling deionized water for 30 min and the procedure was repeated at least twice to remove the sulfuric acid completely. On completing the purification procedure, the membrane was stored in 1 M H_2SO_4 at room temperature prior to use.

A single-stack fuel cell was assembled from a membrane/electrode assembly, two stainless steel plates with flow manifolds on the supply sides for gas and water, and two Teflon gaskets. The anode was a 1 cm^2 20% Pt-on-carbon black (Alfa Aesar Co., HiSPEC 3000) electrode with a platinum loading of 0.8 mg cm^{-2}. The cathode was prepared from a suspension containing (70%) of catalyst, (30%) of 5 wt% Nafion (Sigma Aldrich) recast solution, and ethanol, which had been ultrasonically blended for 1 h to form a uniform and homogenous ink. The suspension ink was spread uniformly across the surface of a carbon paper substrate followed by drying in a vacuum oven at 80 °C for 2 h. For a cathode area of 1 cm^2, the amount of catalyst suspension applied to the cathode was 2.7 mg cm^{-2} of Cu and 1.8 mg cm^{-2} of Pt. A single cell assembly was prepared by sandwiching a Nafion 1135 membrane between the cathode and the anode and was pressed by the stainless steel plates. The cell was connected to a conventional gas flow system. Pure H_2 was introduced to the anode compartment and O_2 was introduced to the cathode compartment. Flow rates of the cathode and anode gases were controlled by mass-flow valves (40 mL min^{-1}). The fuel-cell reaction was

operated at 80 °C. A current–potential curve was measured by a digital multimeter (GDM-8145) and DC Electronic Load (0–360 V/150 W).

Supporting Information

Supporting Information is available from the Wiley Online Library or from the author.

Acknowledgements

K.P.L. thanks an MOE Tier 2 grant "Interface Engineering of Graphene Hybrids for Energy Conversion (R-143-000-488-112)" for funding support.

Received: February 7, 2013
Revised: March 16, 2013
Published online: May 21, 2013

[1] J. Suntivich, H. A. Gasteiger, N. Yabuuchi, H. Nakanishi, J. B. Goodenough, Y. Shao-Horn, *Nat. Chem.* **2011**, *3*, 546.
[2] X. Wang, K. Maeda, A. Thomas, K. Takanabe, G. Xin, J. M. Carlsson, K. Domen, M. Antonietti, *Nat. Mater.* **2008**, *8*, 76.
[3] O. Khaselev, J. A. Turner, *Science* **1998**, *280*, 425.
[4] L. Qu, Y. Liu, J. B. Baek, L. Dai, *ACS Nano* **2010**, *4*, 1321.
[5] A. Morozan, B. Jousselme, S. Palacin, *Energy Environ. Sci.* **2011**, *4*, 1238.
[6] Q. Xiang, J. Yu, M. Jaroniec, *Chem. Soc. Rev.* **2012**, *41*, 782.
[7] M. Pumera, *Chem. Soc. Rev.* **2010**, *39*, 4146.
[8] J. Hou, Y. Shao, M. W. Ellis, R. B. Moore, B. Yi, *Phys. Chem. Chem. Phys.* **2011**, *13*, 15384.
[9] D. R. Dreyer, S. Park, C. W. Bielawski, R. S. Ruoff, *Chem. Soc. Rev.* **2010**, *39*, 228.
[10] M. D. Allendorf, A. Schwartzberg, V. Stavila, A. A. Talin, *Chem. Eur. J.* **2011**, *17*, 11372.
[11] C. Petit, T. J. Bandosz, *Adv. Mater.* **2009**, *21*, 4753.
[12] M. Jahan, Q. L. Bao, J. X. Yang, K. P. Loh, *J. Am. Chem. Soc.* **2010**, *132*, 14487.
[13] M. Jahan, Q. L. Bao, K. P. Loh, *J. Am. Chem. Soc.* **2012**, *134*, 6707.
[14] S. K. Lee, S. D. George, W. E. Antholine, B. Hedman, K. O. Hodgson, E. I. Solomon, *J. Am. Chem. Soc.* **2002**, *124*, 6180.
[15] K. D. Karlin, A. Zuberbühler, J. Reedijk, E. Bouwman, *Bioinorg. Catal.* **1999**, 469.
[16] I. Bento, M. A. Carrondo, P. F. Lindley, *J. Biol. Inorg. Chem.* **2006**, *11*, 539.
[17] A. Zaky, F. Assaf, *Br. Corros. J.* **2002**, *37*, 48.
[18] J. Gomez Becerra, R. Salvarezza, A. Arvia, *Electrochim. Acta* **1988**, *33*, 613.
[19] C. H. Pyun, S. M. Park, *J. Electrochem. Soc.* **1986**, *133*, 2024.
[20] S. Cheng, M. Gattrell, T. Guena, B. MacDougall, *Electrochim. Acta* **2002**, *47*, 3245.
[21] G. E. Badea, *Electrochim. Acta* **2009**, *54*, 996.
[22] G. A. Rance, D. H. Marsh, R. J. Nicholas, A. N. Khlobystov, *Chem. Phys. Lett.* **2010**, *493*, 19.
[23] B. Reed, M. Sarikaya, *Phys. Rev. B: Condens. Matter.* **2001**, *64*, 195404.
[24] J. Paredes, S. Villar-Rodil, A. Martinez-Alonso, J. Tascon, *Langmuir* **2008**, *24*, 10560.
[25] X. Sun, Z. Liu, K. Welsher, J. T. Robinson, A. Goodwin, S. Zaric, H. Dai, *Nano Res.* **2008**, *1*, 203.
[26] S. M. Islam, A. S. Roy, P. Mondal, S. Paul, N. Salam, *Inorg. Chem. Commun.* **2012**, *24*, 170.
[27] a) S. Gupta, S. Pal, A. K. Barik, A. Hazra, S. Roy, T. N. Mandal, S. M. Peng, G. H. Lee, M. Salah El Fallah, J. Tercero, *Polyhedron* **2008**, *27*, 2519; b) A. Barik, B. Mishra, A. Kunwar, R. M. Kadam, L. Shen, S. Dutta, S. Padhye, A. K. Satpati, H. Y. Zhang, K. Indira Priyadarsini, *Eur. J. Med. Chem.* **2007**, *42*, 431.
[28] a) D. Li, M. B. Müller, S. Gilje, R. B. Kaner, G. G. Wallace. *Nat. Nanotechnol.* **2008**, *3*, 101; b) E.-Y. Choi, T. H. Han, J. Hong, J. E. Kim, S. H. Lee, H. W. Kim, S. O. Kim, *J. Mater. Chem.* **2010**, *20*, 1907; c) C. Zhang, L. Ren, X. Wang, T. Liu, *J. Phys. Chem. C* **2010**, *114*, 11435.
[29] D. N. Dybtsev, H. Chun, K. Kim, *Angew. Chem.* **2004**, *116*, 5143.
[30] a) S. A. Bourne, J. Lu, A. Mondal, B. Moulton, M. J. Zaworotko, *Angew. Chem., Int. Ed.* **2001**, *40*, 2111; b) R. Kitaura, F. Iwahori, R. Matsuda, S. Kitagawa, Y. Kubota, M. Takata, T. C. Kobayashi, *Inorg. Chem.* **2004**, *43*, 6522.
[31] a) P. Karthika, N. Rajalakshmi, K. S. Dhathathreyan, *Soft Nanosci. Lett.* **2012**, *2*, 59; b) H.-K. Jeong, Y. P. Lee, R. J. W. E. Lahaye, M.-H. Park, K. H. An, I. J. Kim, C.-W. Yang, C. Y. Park, R. S. Ruoff, Y. H. Le, *J. Am. Chem. Soc.* **2008**, *130*, 1362.
[32] Y. G. Li, H. L. Wang, L. M. Xie, Y. Y. Liang, G. S. Hong, H. J. Dai, *J. Am. Chem. Soc.* **2011**, *133*, 7296.
[33] P. D. Tran, M. Nguyen, S. S. Pramana, A. Bhattacharjee, S. Y. Chiam, J. Fize, M. J. Field, V. Artero, L. H. Wong, J. Loo, J. Barber, *Energy Environ. Sci.* **2012**, *5*, 8912.
[34] J. L. Zhang, M. B. Vukmirovic, K. Sasaki, A. U. Nilekar, M. Mavrikakis, R. R. Adzic, *J. Am. Chem. Soc.* **2005**, *127*, 12480.
[35] P. Sotelo-Mazón, R. González-Huerta, J. Cabañas-Moreno, O. Solorza-Feria *Int. J. Electrochem. Sci.* **2007**, *2*, 523.
[36] A. Ocampo, R. Castellanos, P. Sebastian, *J. New Mater. Electrochem. Syst.* **2002**, *5*, 163.
[37] J. Prakash, D. A. Tryk, E. B. Yeager, *J. Electrochem. Soc.* **1999**, *146*, 4145.
[38] A. Damjanovic, V. Brusic, *Electrochim. Acta* **1967**, *12*, 615.
[39] A. Damjanovic, M. A. Genshaw, *Electrochim. Acta* **1970**, *15*, 1281.
[40] A. Riddiford, *Electrochim. Acta* **1961**, *4*, 170.
[41] W. Song, J. Hou, H. Yu, L. Hao, Z. Shao, B. Yi, *Int. J. Hydrogen Energy* **2008**, *33*, 4844.
[42] Y. Nabae, I. Yamanaka, K. Otsuka, *Appl. Catal., A* **2005**, *280*, 149.
[43] F. R. Brushett, M. S. Thorum, N. S. Lioutas, M. S. Naughton, C. Tornow, H. R. M. Jhong, A. A. Gewirth, P. J. A. Kenis, *J. Am. Chem. Soc.* **2010**, *132*, 12185.
[44] R. Bashyam, P. Zelenay, *Nature* **2006**, *443*, 63.
[45] F. Charreteur, F. Jaouen, S. Ruggeri, J. P. Dodelet, *Electrochim. Acta* **2008**, *53*, 2925.
[46] Z. Chen, D. Higgins, A. Yu, L. Zhang, J. Zhang, *Energy Environ. Sci.* **2011**, *4*, 3167.
[47] Y. Gorlin, T. F. Jaramillo, *J. Am. Chem. Soc.* **2010**, *132*, 13612.
[48] Y. Liang, Y. Li, H. Wang, J. Zhou, J. Wang, T. Regier, H. Dai *Nat. Mater.* **2011**, *10*, 780.
[49] M. H. Miles, G. Kissel, P. W. T. Lu, S. Srinivasan, *J. Electrochem. Soc.* **1976** *123*, 332.
[50] H. B. Martin, A. Argoitia, U. Landau, A. B. Anderson, J. C. Angus, *J. Electrochem. Soc.* **1996**, *143*, L133.
[51] C. Petit, B. Mendoza, T. J. Bandosz, *Langmuir* **2010**, *26*, 15302.
[52] C. Petit, J. Burress, T. J. Bandosz, *Carbon* **2011**, *49*, 563.
[53] C. Petit, T. J. Bandosz, *Adv. Funct. Mater.* **2011**, *21*, 2108.
[54] C. Petit, T. J. Bandosz, *Dalton Trans.* **2012**, *41*, 4027.